Article

Functional Materials Design via Structural Regulation Originated from Ions Introduction: A Study Case in Cesium Iodate System

Min Zhang, Cong Hu, Tushagu Abudouwufu, Zhihua Yang, and Shilie Pan

Chem. Mater., **Just Accepted Manuscript** • DOI: 10.1021/acs.chemmater.7b05252 • Publication Date (Web): 18 Jan 2018

Chemistry of Materials is published by the American Chemical Society. 1155 Sixteenth Street N.W., Washington, DC 20036

Functional Materials Design via Structural Regulation Originated from Ions Introduction: A Study Case in Cesium Iodate System

Min Zhang,[†, #] Cong Hu,[†, ‡, #] Tushagu Abudouwufu,[†, ‡] Zhihua Yang, [†,*] Shilie Pan[†,*]

†Key Laboratory of Functional Materials and Devices for Special Environments, Xinjiang Technical Institute of Physics & Chemistry, Chinese Academy of Sciences; Xinjiang Key Laboratory of Electronic Information Materials and Devices, 40-1 South Beijing Road, Urumqi 830011, China

‡University of the Chinese Academy of Sciences, Beijing 100049, China

# These authors contributed equally.

ABSTRACT:

Tailored structural regulation to achieve novel compounds with special properties is very attractive and important for functional material design. In this paper, $CsIO_3$ was selected as a maternal structure and three new derivatives, namely, $CsIO_2F_2$, $Cs_3(IO_2F_2)_3 \cdot H_2O$ and $Cs(IO_2F_2)_2 \cdot H_5O_2$ were successfully prepared by introducing different units (F^-, H_2O, $H_5O_2^+$ and $IO_2F_2^-$) under hydrothermal condition for the first time. Then the structural transformations were schematically analyzed and the corresponding properties originated from ions introduction were investigated. Therein, noncentrosymmetric $CsIO_3$ and $CsIO_2F_2$ exhibit good nonlinear optical properties with large second harmonic generation (SHG) effects (15 × and 3 × KH_2PO_4), wide band gaps (4.2 and 4.5 eV), wide transmittance ranges (~0.27-5.5 μm), and high laser damage thresholds (15 × and 20 × $AgGaS_2$, respectively), which shows that they are potential nonlinear optical materials in near-ultraviolet to mid-infrared. To further analyze the structure-properties relationship, the first-principle calculations are applied to explore the origins of the optical properties, such as birefringences and SHG responses. Moreover, the protonated $(H_5O_2)^+$ cations in $Cs(IO_2F_2)_2 \cdot H_5O_2$ implies that it may feature enhanced conductivity, which was tentatively verified by the resistivity tests via the conventional *dc* four-probe method. The study case of structural regulation realized by ions introduction in this work may give a feasible guidance for functional materials design.

1. INTRODUCTION

Since the properties of materials significantly depend on their structures, many researchers endeavor themselves to explore the feasible ways to tailor structural regulation, and anticipate to design new crystals with novel structures and excellent properties.[1-8] Recent decades, great progresses and achievements have been made in the rational design of functional materials, especially in the fields of organic (or organic-inorganic) chemistry[9-11] and nanochemistry,[12] *etc*. While the structural design of inorganic functional materials are still in the exploratory period because of the poor controllability.[13-21] For the iodates, extensive researches have been executed and numerous new compounds with special functional properties benefitting from

nonbonding, but stereochemically active, pair of electrons from iodine have been designed.[22-26] Up to now, iodates have become a crucial branch of inorganic functional materials in various application fields, such as nonlinear optical (NLO),[22-27] luminescent,[28,29] energetic [30,31] and photocatalytic materials,[32,33] *etc*. After decades of development, iodates went through from the period of classical alkali metal iodates[34-36] to iodates combined with other metal cations,[37-40] such as, lone-pair containing,[41-43] d^0 transition metals,[44,45] *etc*., or organic molecules,[46] which greatly enrich the researches of iodates system in the aspects of structures, syntheses, properties and applications.

From the chemical design point of view, second-order NLO materials based on metal iodates are excellent candidates for the rational synthesis, since the natural instinct of the asymmetric I-O/F units could serve as a structure-directing agent and are beneficial to generate the noncentrosymmetric (NCS) macrostructures.[47,48] Also, NCS iodates can satisfy the basic requirements for NLO application, such as large second harmonic generation (SHG) efficiency, wide transparency range from visible or even UV (beneficial to improve laser damage threshold (LDT)) to mid-infrared ranges, moderate birefringence to satisfy the phase matching behaviors, *etc*.[49] Moreover, metal iodates can be synthesized and grown as large crystals by aqua-solution or mild hydrothermal methods at relatively low temperature (< 250 ^{o}C) with short growth time (< one week). In the process of tailored synthesis of alkali metal iodates/fluoroiodates, various monovalent ions or units, such as A^+ (A = alkali metal), F^-, OH^-, $(IO_3)^-$, $(IO_2F_2)^-$ and $H^+(H_2O)_n$ ($n \geq 0$), *etc*.,[50-53] could participate in chemical reaction and promote the formation of targeted compounds like assembling the toy building blocks. This provides an effective research system to chemically and structurally investigate the structure regulation by introducing the ions.

In this article, the cesium iodate $CsIO_3$, analog to the classical NLO material α-$LiIO_3$, was selected as a maternal structure to start our researches. Finally, $CsIO_3$ single crystal and other three new derivatives, $CsIO_2F_2$, $Cs_3(IO_2F_2)_3{\cdot}H_2O$ and $Cs(IO_2F_2)_2{\cdot}H_5O_2$ were synthesized via the introduction of ions using hydrothermal method for the first time. Structural evolution schematically occurs among them *via*

introduction of F^-, H_2O, $(IO_2F_2)^-$ and $(H_5O_2)^+$ units, then the arrangement of fundamental building blocks (FBB) and symmetry consequently changed. The NLO properties of NCS $CsIO_3$ and $CsIO_2F_2$ were firstly researched and the results promise $CsIO_3$ and $CsIO_2F_2$ as potential NLO materials because of the large SHG responses and high LDTs. Interestingly, the protonated $(H_5O_2)^+$ cations were found in $Cs(IO_2F_2)_2 \cdot H_5O_2$ implies that it may feature enhanced conductivity.[54-56]

2. EXPERIMENAL SECTION

2.1 Syntheses and Crystal Growth.

All the starting materials, Cs_2CO_3 (AR, 99.9 %, Xinjiang Nonferrous Metal Group), HIO_3 (AR, 99.5 %, Aladdin) and hydrofluoric acid (40 %, Aladdin) were commercially available and used as received.

Polycrystalline powder of $CsIO_3$ was directly obtained by liquid phase reaction. Cs_2CO_3 and HIO_3 in a molar ratio of 1:2 were mixed with moderate amount of deionized water under continuous grinding at room temperature, then air-dried to obtain the $CsIO_3$ phase. The single crystal of mentioned compounds was synthesized by traditional hydrothermal reactions at 220 °C using synthesized $CsIO_3$ powder as initial reactant (Figure 1). Specifically, 2 mmol (0.6156 g) $CsIO_3$ were transferred to 23 ml Teflon-lined autoclave, then 2 ml H_2O (for $CsIO_3$), 1 ml HF (for $CsIO_2F_2$), 2mmol (0.3518 g) HIO_3 combined with 1 ml HF and 1 ml H_2O (for $Cs(IO_2F_2)_2 \cdot H_5O_2$) were added into the corresponding autoclaves, respectively, and subsequently sealed. The autoclaves were heated to 220 ^oC, held for 4 days, and slowly cooled to room temperature at a rate of 3 $^oC \cdot h^{-1}$. After that, the crystals in autoclaves were filtrated and air-dried for further characterization. It was failed to prepare $Cs_3(IO_2F_2)_3 \cdot H_2O$ using $CsIO_3$ as initial reactant, and $Cs_3(IO_2F_2)_3 \cdot H_2O$ was successfully obtained by the optimal ratio of 2 mmol (0.6516 g) Cs_2CO_3, 2 mmol (0.3518 g) HIO_3 and 2 ml HF. Moreover, above crystals also can be obtained by solvent evaporation method at room temperature using the clear solution after filtration, which implies that sizable crystals can be prepared by optimizing the crystal growth parameters. The purities of samples were characterized via powder X-ray diffraction analyses (Figure S1 in the Supporting Information, SI).

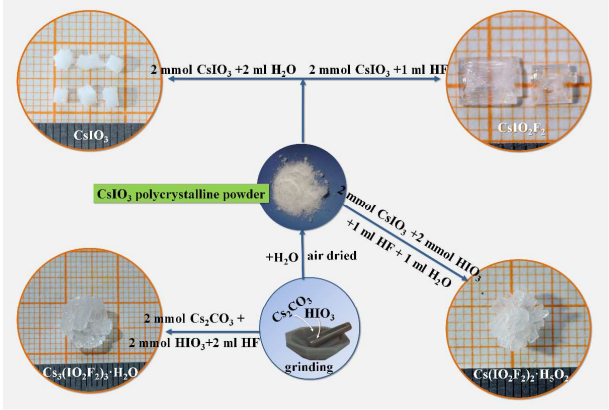

Figure 1. Schematic diagram of synthetic process of $CsIO_3$, $CsIO_2F_2$, $Cs_3(IO_2F_2)_3 \cdot H_2O$ and $Cs(IO_2F_2)_2 \cdot H_5O_2$ via hydrothermal method.

2.2 Powder X-ray Diffraction.

Powder X-ray diffraction (PXRD) measurements for as-prepared compounds were carried out on a Bruker D2 PHASER diffractometer equipped with Cu Kα radiation at room temperature. The 2θ range is 10–70° with a step size of 0.02° and a fixed counting time of 1 s/step.

2.3 Structure Determination.

Single crystal XRD data of four crystals were collected on a Bruker SMART APEX II 4K CCD diffractometer at 296(2) K using Mo Ka radiation (λ = 0.71073 Å) and integrated with a SAINT–Plus program.[57] The crystal structures were solved by direct methods and refined in the SHELXTL system.[58] Final least-squares refinement on F_o^2 with data having $F_o^2 \geq 2\sigma(F_o^2)$ includes anisotropic displacement parameters for all atoms. The structures were checked for missing symmetry elements with PLATON,[59] and no higher symmetries were found. The structures of hydrogen containing compounds were optimized based on first principle calculation. Microprobe element analyses of four compounds were performed on an energy-dispersive X-ray spectroscope (EDS, OXFORD 2000) to verify the absence or presence of fluorine. The EDS analyses show that the Cs: I: O: F molar ratios are 1.00:1.12:3.33:0, 1.00:0.92:1.86:1.91, 1.00:0.98:2.10:1.95, and 1.00:1.89:5.51:3.65, for $CsIO_3$, $CsIO_2F_2$, $Cs_3(IO_2F_2)_3 \cdot H_2O$ and $Cs(IO_2F_2)_2 \cdot H_5O_2$, respectively, which verifies the calculated structure model. Relevant crystallographic information is given in Table 1. The atomic

coordinates and the equivalent isotropic displacement parameters are summarized in Table S1, selected bond lengths and angles are listed in Table S2.

2.4 Thermal Behavior Analyses.

The thermal behaviors of four compounds were investigated with thermogravimetry and differential scanning calorimeter (TG-DSC) using a NETZSCH STA 449F3 simultaneous thermal analyzer. The samples were placed in a Pt crucible and heated at a rate of 5 ^{o}C min^{-1} in the range of 40–1000 ^{o}C under a flow of nitrogen gas.

2.5 Vibrational Spectroscopy and Optical Properties.

The infrared spectroscopies were carried out on a Shimadzu IRAffinity-1 spectrometer in order to specify and compare the coordination of I-O/F atoms and hydrogen bond in title compounds. The samples were mixed with dried KBr (about 5 mg samples mix with 500 mg KBr), and collected in the range from 400 to 4000 cm^{-1} with a resolution of 2 cm^{-1}. Moreover, the infrared spectrum of $CsIO_2F_2$ was also tested on as-grown crystal plate to determine the transmittance cutoff edge in infrared region. Raman spectra were characterized using LABRAM HR Evolution spectrometer equipped with a CCD detector by a 532 nm laser, and the integration time was set to be 10 s. UV-vis-NIR diffuse-reflectance data of compounds were collected at RT using polytetrafluoroethylene as a standard on a Shimadzu SolidSpec-3700DUV Spectrophotometer with the measurement range extended from 190 to 2600 nm, and the Kubelka−Munk function was used to convert the reflectance spectra to the absorbance data.[60]

2.6 Powder Second-harmonic Generation Measurements.

The powder SHG measurements were carried out on the basis of the Kurtz–Perry method[35] at room temperature on a Q-switched Nd:YVO_4 solid-state laser at a wavelength of 1064 nm (10 ns, 10 KHz). Since the SHG intensities show strong dependence on the particle sizes, polycrystalline samples were ground and sieved into the following particle size ranges: <20, 20–38, 38–55, 55–88, 88–105, 105–150 and 150–200 μm. The samples were pressed between glass slides and secured with tapes in 1-mm thick aluminum holders containing an 8-mm diameter hole, then placed into a light-tight box and irradiated with the laser. The intensities of the frequency-doubled

output emitted from the samples were collected by a photomultiplier tube and recorded using oscilloscope. The commercial NLO crystal KDP was also ground and sieved into the same particle size to make reference.

2.7 LDT Measurements.

The LDTs[4,25,61] of $CsIO_3$ and $CsIO_2F_2$ NLO crystals were evaluated on powder sample (< 20 μm) with a pulsed Nd:YAG laser (1064 nm, 10 ns, 10 Hz), and the same size of $AgGaS_2$ was chosen as the reference. With the increasing of laser energies, the color changes of the powder samples were constantly observed by optical microscope to determine the damage threshold, and the damage spots were measured by the scale of optical microscope. To adjust different laser beams, an optical concave lens was added into the laser path.

2.8 Numerical Calculation Details.

The theoretical simulations of the electronic structures and optical properties were performed by the plane wave pseudopotential method based on the density functional theory (DFT)[62] implemented in the CASTEP package[63]. Perdew-Burke-Ernzerhof (PBE) functional with the generalized gradient approximation (GGA)[64] and norm-conserving pseudopotential (NCP)[65] were adopted with the energy cutoffs of (750, 850, 850, 850 eV, respectively) and the Brillouin zone (BZ) Monkhorst-Pack grids of (4 × 4 × 4, 3 × 3 × 3, 1 × 2 × 3, 1 × 2 × 3, respectively) among the calculations of $CsIO_3$, $CsIO_2F_2$, $Cs_3(IO_2F_2)_3 \cdot H_2O$ and $Cs(IO_2F_2)_2 \cdot H_5O_2$.

3. RESULTS AND DISCUSSION

3.1 Crystal Structure Descriptions.

The structure of $CsIO_3$ was successively solved as CS cubic space group of *Pm*-3*m* and NCS monoclinic *Pm* space group in 1928 and 1985 using powder X-ray diffraction data, respectively.[66] The inaccurate space group analysis was caused by pseudocubic features,[67] so the crystal structures and properties of $CsIO_3$ were re-investigated in this work. The single crystal structure of $CsIO_3$ was determined for the first time. $CsIO_3$ crystallizes in an NCS trigonal *R*3*m* (160) space group with a = 6.6051(10) Å and c = 8.087(3) Å. The asymmetric unit of $CsIO_3$ contains one, one

and one crystallographic independent Cs, I, and O atoms, respectively. As shown in Figure 2a, isolated $(IO_3)^-$ units connect with the CsO_{12} polyhedra to form the whole structure.

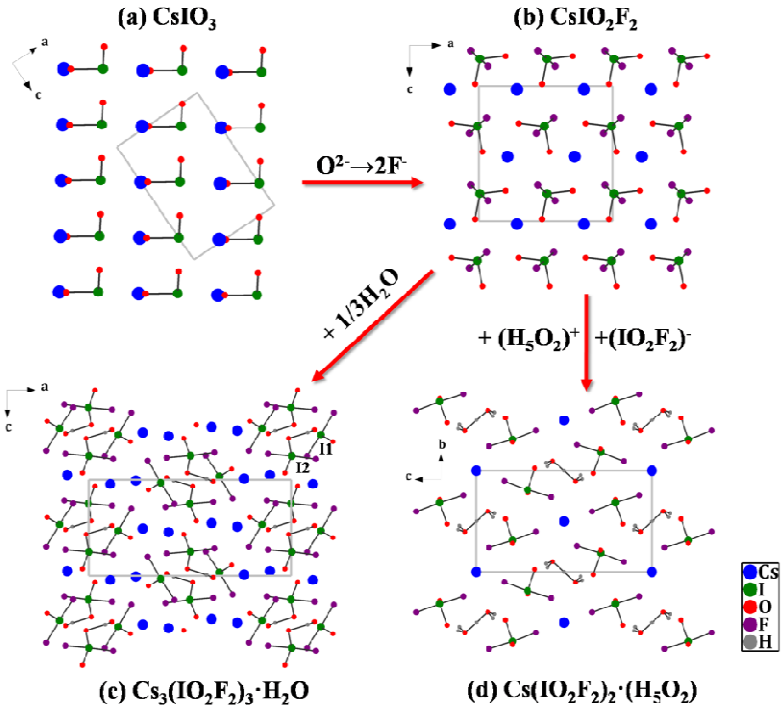

Figure 2. Schematic diagrams of structural evolution among (a) $CsIO_3$, (b) $CsIO_2F_2$, (c) $Cs_3(IO_2F_2)_3{\cdot}H_2O$ and (d) $Cs(IO_2F_2)_2{\cdot}H_5O_2$. The Cs–O/F bonds are removed for clarity.

$CsIO_2F_2$ has an orthorhombic crystal lattice with NCS space group $Pca2_1$. The asymmetric unit of $CsIO_2F_2$ consists one Cs, one I, two O, and two F atoms, respectively. The FBB $(IO_2F_2)^-$ results from the substitution of one O^{2-} in $(IO_3)^-$ by two F^- anions (Figure 2b). Similarly, isolated $(IO_2F_2)^-$ units combine with the CsO_3F_5 polyhedra to form the structure of $CsIO_2F_2$.

$Cs_3(IO_2F_2)_3{\cdot}H_2O$ crystallizes in orthorhombic crystal system with CS space group *Pnma* (Figure 2c). There are two Cs, two I, four O, four F, and one H atoms, respectively in the asymmetric unit. The $(IO_2F_2)^-$ units and 1/3 molar ratio of H_2O insert into the tunnels of the CsOF framework forming the integral structure.

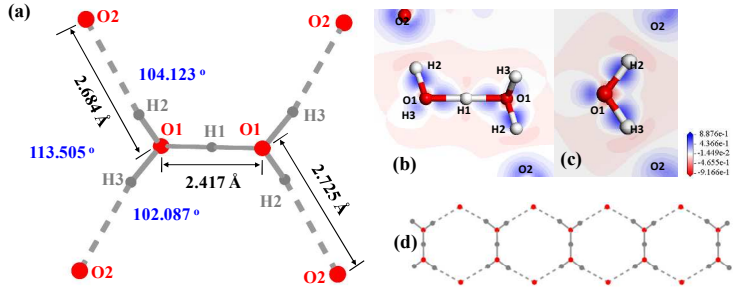

Figure 3. Geometries of $(H_5O_2)^+$ in $Cs(IO_2F_2)_2{\cdot}H_5O_2$. (a) Distances and angles of the O atoms between $H_5O_2^+$ (O1) and fluoroiodate oxygens (O2); (b) 1D chain structure formed via the connection of hydrogen bonds and $H_5O_2^+$ units; (c) and (d) Differential charge density of the $(H_5O_2)^+$ unit.

The centrosymmetric $Cs(IO_2F_2)_2{\cdot}H_5O_2$ with space group of $P2_1/c$ has one unique Cs, one unique I, three unique O, two unique F, and three unique H atoms, respectively in the asymmetric unit. Therein, two O(1) atoms and three H atoms connect with each other to form a protonated $(H_5O_2)^+$, which further combines with isolated $(IO_2F_2)^-$ via hydrogen bonds, generating a $[(IO_2F_2)_2{\cdot}H_5O_2]^-$ polymeric chain along *a* direction. Then $[(IO_2F_2)_2{\cdot}H_5O_2]^-$ chains connect with the Cs-O/F polydedra to form the whole structure (Figure 2d). The coordinations of the H atoms in $(H_5O_2)^+$ were primarily deduced based on the extremely low (+0.087) bond valence sum (BVS)[68,69] of O1 oxygen. The electron density difference around the hydrogen bonds of O1-H1-O1 exhibits a unique distribution as a sandglass, which is apparently different from those of O1-H3⋯O2. Moreover, the geometric position of the O atoms between $(H_5O_2)^+$ (O1) and fluoroiodate oxygens (O2) shows a short O1-O1 distance about 2.4 Å and O1-O2 distances are about 2.684-2.725 Å (Figure 3),which agree well with the reported geometries of the O atoms around $(H_5O_2)^+$,[70] such as, precisely determined structure of $V(H_2O)_6(H_5O_2)(CF_3SO_3)_4$ using X-ray and neutron diffraction,[71] verifying the validity of $(H_5O_2)^+$ configuration.

The iodine atoms in above four compounds are three- or four-coordinated, respectively. Therein, the I–O and I–F distances of $(IO_2F_2)^-$ in $CsIO_2F_2$, $Cs_3(IO_2F_2)_3{\cdot}H_2O$ and $Cs(IO_2F_2)_2{\cdot}H_5O_2$ are very similar, and lie in the range of 1.75-1.82 Å and 1.95-2.01 Å, respectively. The BVS (bond valence parameter R_{ij} =

2.007 and B = 0.37 for I^{5+}–O^{2-})[68] of the I atom using Brown's formula is calculated to be 5.39, 5.22 (and 5.05), 5.19 for $CsIO_2F_2$, $Cs_3(IO_2F_2)_3 \cdot H_2O$ and $Cs(IO_2F_2)_2 \cdot H_5O_2$, respectively (Table S2 in the SI), which are close to the ideal oxidation state of iodine cation (5+) and further prove that the coordination of the I atom is reasonable. While the I–O bond lengths of $(IO_3)^-$ in $CsIO_3$ are all equal to 1.889(16) Å, which are much larger than the I–O bond lengths in isostructural $RbIO_3$ (all equal to 1.73(3) Å).[63] Although the I–O bond lengths are very closed to the usual ranges, simultaneously small (or large) distances lead to abnormal BVS value of the I atoms in $CsIO_3$ (4.05) and $RbIO_3$ (6.27).

3.2 Exploration of Structural Transformation.

Since the functional motifs in four compounds are isolated, the Cs-O/F framework are analyzed using topological approach to further explore the structure evolution manipulated by ions introduction. The topological crystal structures are schematically shown in Figure 4. Therein, differently coordinated CsO/F polyhedra in title compounds are regarded as connection nodes, and different dimensional Cs-O/F frameworks are obviously found in them. Specifically, when one O^{2-} in $(IO_3)^-$ is substituted of by two F^-, the Cs-O 3D framework of $CsIO_3$ was broken and transforms into 2D Cs-O/F layers in $CsIO_2F_2$ extending in *ac* plane with the distances between layers about 6.377 Å. Moreover, the introduction of 1/3 molar ratio of H_2O into $CsIO_2F_2$ generates a 3D Cs-O/F framework containing a tunnel with a shortest diameter of about 7.498 Å in $Cs_3(IO_2F_2)_3 \cdot H_2O$. Meanwhile, dimensionality reduction occurs from 2D Cs-O/F layers in $CsIO_2F_2$ to 1D Cs-O/F chains in $Cs(IO_2F_2)_2 \cdot H_5O_2$ during the simultaneous introduction of $(H_5O_2)^+$ and $(IO_2F_2)^-$. Above mentioned compounds can be described in the topological view[72] with the Schläfli symbol of $3^{60} \cdot 4^{87} \cdot 5^6$ 3D 18-*c* (connected) network and $3^6 \cdot 4^6 \cdot 5^3$ 6-*c* uninodal *hxl*/Shubnikov plane net for $CsIO_3$ and $CsIO_2F_2$, respectively. Two-nodal 7-*c* (Cs1) and 8-*c* (Cs2) net with stoichiometry of 1:2 is obtained in $Cs_3(IO_2F_2)_3 \cdot H_2O$, and the Schläfli symbol can be presented as $(3^7 \cdot 4^8 \cdot 5^9 \cdot 6^4)(3^7 \cdot 4^9 \cdot 5^5)_2$. No circuits are found between the Cs nodes because only Cs-O/F chains exist in $Cs(IO_2F_2)_2 \cdot H_5O_2$.

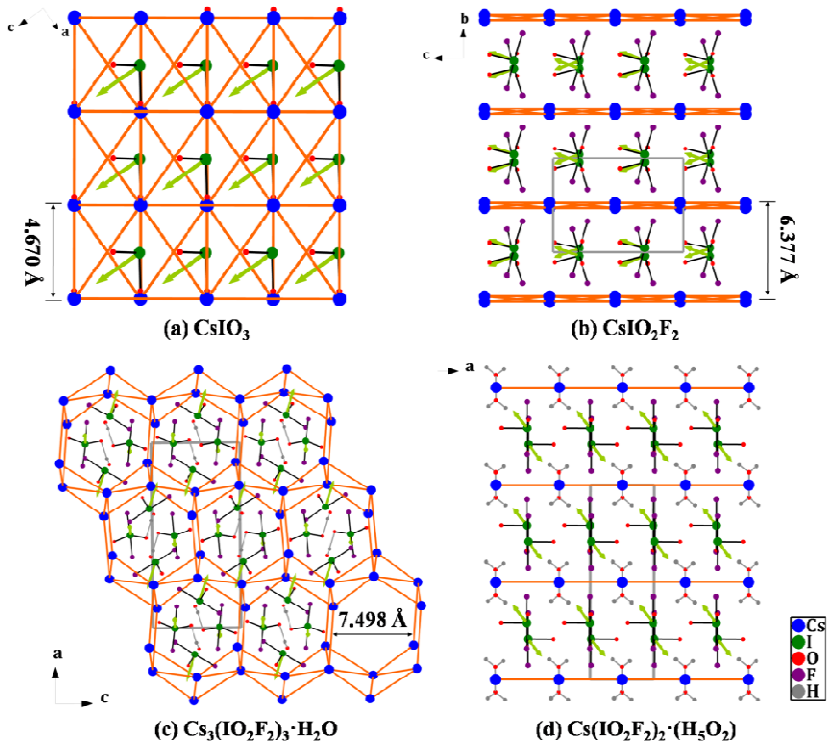

Figure 4. Schematic diagrams of topologically structural evolution among (a) $CsIO_3$, (b) $CsIO_2F_2$, (c) $Cs_3(IO_2F_2)_3{\cdot}H_2O$ and (d) $Cs(IO_2F_2)_2{\cdot}H_5O_2$. The Cs atoms are considered as connection nodes. Dipole moments directions and magnitudes of the IO_3 and IO_2F_2 units are indicated by light green arrows.

Therein, large distorted $(IO_3)^-$ and $(IO_2F_2)^-$ units containing stereochemically active pair of electrons feature well ordered alignments, which may significantly enhance the macroscopic SHG responses and generate NCS $CsIO_3$ and $CsIO_2F_2$ with excellent NLO properties. The calculated dipole moments of the $(IO_3)^-$ units in $CsIO_3$ are 13.428 debye (D), and the values of $(IO_2F_2)^-$ decrease to 11.9–12.3 D in other three fluoroiodates (Table S3 in the SI), which are consistent with those of the other reported metal iodates and fluoroiodates.[73] Because of the well-aligned $(IO_3)^-$ units in $CsIO_3$, the total dipole moments are perfectly enhanced (0.396×10^{-18} esu·cm/Å^3), and are larger than those of $CsIO_2F_2$ (0.272×10^{-18} esu·cm/Å^3). Hence, we can tentatively deduce that the SHG response of $CsIO_3$ may be stronger than that of $CsIO_2F_2$. For $Cs(IO_2F_2)_2{\cdot}H_5O_2$, protonated $(H_5O_2)^+$ ions stabilized by short, strong, low-barrier (SSLB) H-bonds, imply that $Cs(IO_2F_2)_2{\cdot}H_5O_2$ may feature enhanced

conductivity.[56] The supposition is tentatively verified by the resistivity tests of four compounds via the conventional *dc* four-probe method (Figure S2 in the SI), the further characterizations will be executed in future work. It is worth noting that, since the long-ordered structures of $(H_5O_2)^+$ ions in $Cs(IO_2F_2)_2{\cdot}H_5O_2$ are 1D chains (Figure 2b), which may provide a suitable own-channels for proton transfer.[74]

3.3 Thermal Behavior.

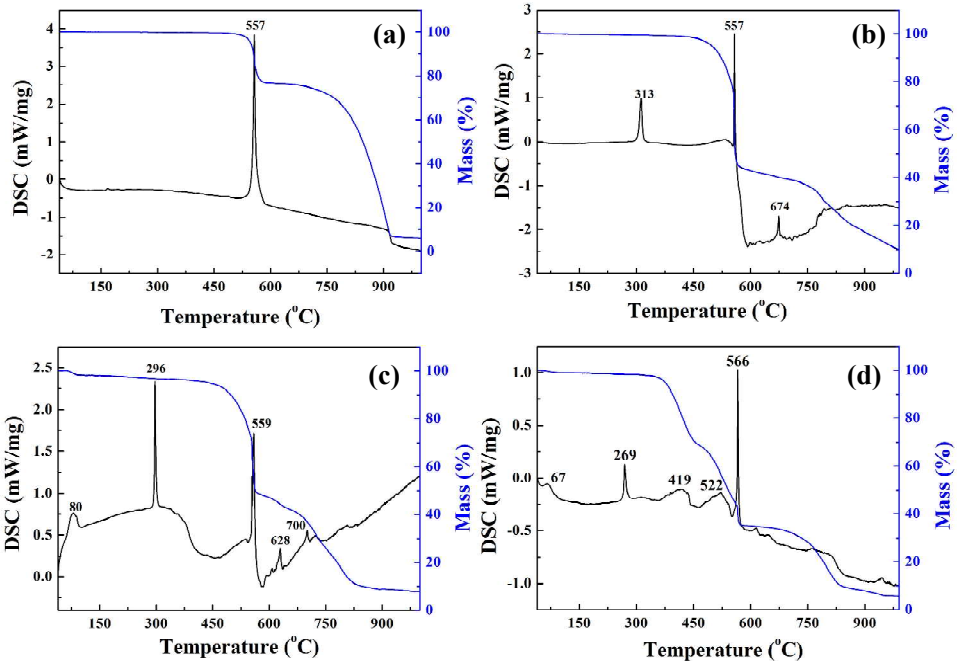

Figure 5. TG-DSC curves of (a) $CsIO_3$, (b) $CsIO_2F_2$, (c) $Cs_3(IO_2F_2)_3{\cdot}H_2O$ and (d) $Cs(IO_2F_2)_2{\cdot}H_5O_2$.

The TG-DSC curves of as-grown crystals are shown in Figure 5. Apparently, there is only one sharp endothermic peak around 557 °C with simultaneous weight loss for $CsIO_3$. Based on the calcine experiments of samples, the decomposition reaction at about 550 °C can be described as $CsIO_3$ decomposes to CsI with the loss of oxygens (Figure S3a in SI). While several obvious endothermic peaks, including two sharp peaks approximately at 300 (without weight loss) and 550 °C (with weight loss), respectively, were found on the DSC curves for three fluoroiodates. Specifically, $CsIO_2F_2$ decomposes to $CsIO_3$ and CsF at about 313 °C (Figure S3b in SI), and residual $CsIO_3$ further decomposes to CsI and oxygens at about 557 °C, then cesium

halides melts at about 674 ^{o}C. $Cs_3(IO_2F_2)_3 \cdot H_2O$ starts to dehydrate at about 80 ^{o}C corresponding to the weight loss about 1.73 %, which agrees well with the calculated one (1.79 %), and the following decomposition reaction is very similar with maternal $CsIO_2F_2$. For $Cs(IO_2F_2)_2 \cdot H_5O_2$, dehydration occurs at about 67 ^{o}C and firstly decomposes around 269 ^{o}C without mass loss, then continuously loses weights at about 419, 522 and 566 ^{o}C, respectively, corresponding to the loss of halides and oxygen.

3.5 Vibrational Spectroscopies and Optical Properties.

The infrared spectra and Raman spectra (Figure 6a) were measured to further confirm the I-O/F and hydrogen bonds in the synthesized compounds. The sharp absorption peaks at about 751−796 cm^{-1} in IR spectra of four compounds are mainly attributed to the strong asymmetric stretching vibrations of $(IO_3)^-$ and $(IO_2F_2)^-$,[75,76] which are consistent with the I-O/F vibration at about 745-817 cm^{-1} in Raman spectra. Moreover, compared with the Raman spectra of I-O bonds in $CsIO_3$, the stretching bands of I-F in three fluoroiodates obviously shift to the higher wavenumbers (inset of Figure 6a). The wide peaks around 3430 cm^{-1} and weak peaks nearby 1520-1635 cm^{-1} belong to the stretching bands of ν(OH) and δ(HOH) in $Cs_3(IO_2F_2)_3 \cdot H_2O$ and $Cs(IO_2F_2)_2 \cdot H_5O_2$. The peaks around 1048-1121 cm^{-1} may attribute to O-H$^+$-O stretch in protonated $H_5O_2^+$.[72,77]

In order to precisely determine the transmittance range of $CsIO_2F_2$, the single crystal with size up to 5 × 4 × 1 mm^3 was selected to test the infrared transmittance spectrum (Figure S4 in the SI). The result shows that $CsIO_2F_2$ is transparent in 2.5-5.5 μm, which covers the important parts of mid-infra wavelength of atmospheric window (3-5 μm). Moreover, it is found that if we increase the mass ratios of samples to KBr during the infrared spectra test using polycrystalline powders, the obtained infrared cutoff edges will be gradually close to the results tested by crystal plate. The test methods and results are also verified by some examples of borates, sulfates, vanadates and phosphates, etc., using powder and crystals samples, which may provide a feasible way to tentatively determine the infrared cutoff edges before the sizable crystals are obtained.

The UV-vis-NIR reflectance spectra show that the ultra-violet cut-off edges are at about 292, 272, 275 and 281 nm for $CsIO_3$ and other three fluoroiodates, respectively, corresponding to band gaps of about 4.2, 4.5, 4.5 and 4.4 eV, respectively (Figure 6b). Apparently, the introduction of fluorine enlarges the energy gaps, which are consistent with the experimental results of rubidium-based isostructureal compounds (Figure S5 in the SI).

As potential NLO materials, large band gaps may beneficial to obtain high LDTs. Preliminary measurements of the LDTs were performed on the powder samples of $CsIO_3$ and $CsIO_2F_2$ together with $AgGaS_2$ as the reference. The results indicate that $CsIO_3$ and $CsIO_2F_2$ exhibit large LDTs of 165 and 220 MW/cm^2, respectively, which are much higher than that of benchmark $AgGaS_2$ (11 MW/cm^2). The excellent performances indicate that $CsIO_3$ and $CsIO_2F_2$ are promising candidates for high-power NLO applications in near-ultraviolet to mid IR region.

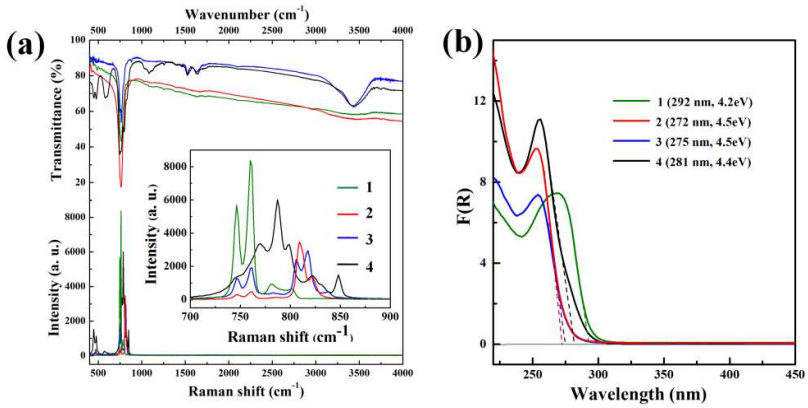

Figure 6. (a) Infrared (top) and Raman spectra (bottom), (b) UV-vis-NIR diffuse reflectance spectra of four compounds. Inset of (a) is the enlarged drawing of Raman spectra.

3.6 Powder SHG Measurements of $CsIO_3$ and $CsIO_2F_2$.

The SHG responses of $CsIO_3$ and $CsIO_2F_2$ under 1064 nm irradiation are performed via the Kurtz−Perry method[35] using a Q-switched Nd:YVO_4 laser. Both of them are type-I phase matchable at 1064 nm according to the Kurtz−Perry rules. As expected, $CsIO_3$ exhibits a very strong SHG response, which is approximately 15 times than that of KDP (Figure 7). It is worth noting that the constantly decreased SHG intensities

were found in the AIO_3 (A = Li, K, Rb, and Cs) series with the increasing of cations radius (Figure S6 in the supporting information). Since the SHG responses mainly come from the well-aligned $(IO_3)^-$ units in the AIO_3 series, the gradual decrease of densities of $(IO_3)^-$ in AIO_3 leads to a decreased SHG responses (0.0151, 0.0131, 0.0107, and 0.0982 $Å^{-3}$ for Li-, K-, Rb-, and Cs-based compounds, respectively.). Although, the SHG response of $CsIO_2F_2$ is smaller than that of $CsIO_3$, the widened band gap and enhanced LDT also prove $CsIO_2F_2$ to be a promising NLO material in higher power laser applications.

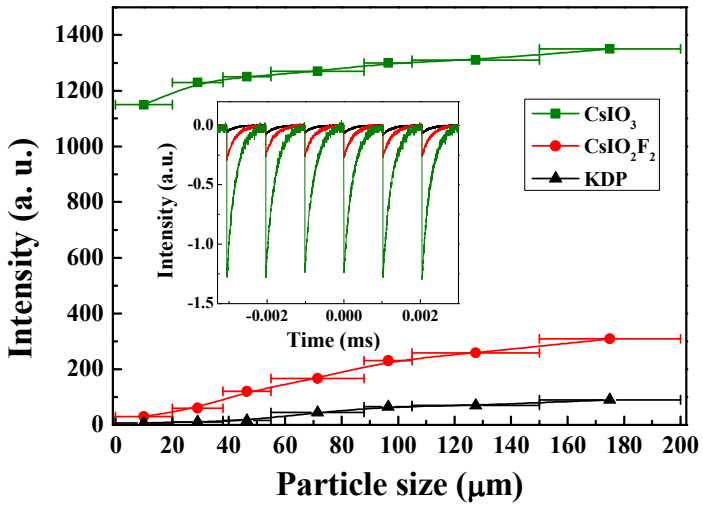

Figure 7. Particle sizes versus SHG intensities of $CsIO_3$, $CsIO_2F_2$ and KDP. Inset is the SHG responses of samples with the particle size of 150-200 μm.

3.7 Theoretical Calculations and Structure-properties Relationships

We calculated the band structures of these four compounds, and the results (Figure S7 in the SI) indicate that $CsIO_3$ and $Cs(IO_2F_2)_2 \cdot H_5O_2$ own direct band gaps of 3.25 and 3.77 eV, while $CsIO_2F_2$ and $Cs_3(IO_2F_2)_3 \cdot H_2O$ own indirect band gaps of 4.15 and 4.37 eV, which are in accordance with the optical experimental band gaps results from the UV-vis-NIR diffuse reflection spectral measurements.

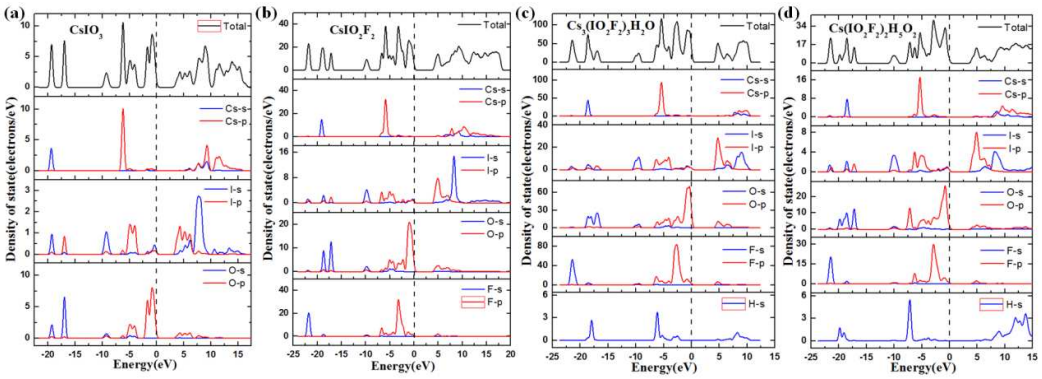

Figure 8. Density of states for (a) $CsIO_3$, (b) $CsIO_2F_2$, (c) $Cs_3(IO_2F_2)_3{\cdot}H_2O$ and (d) $Cs(IO_2F_2)_2{\cdot}H_5O_2$.

The optical behaviors are closely related to the electron transition from valance band (VBs) to conduction bands (CBs), so we present the density of states (DOS) to identify the characteristics of the electronic states. As shown in Figure 8, the VB edge below the Fermi level is mainly composed of O-*p* states with slight I-*s*, *p* and F-*p* states, while the bottle of CBs is occupied by I-*p* states, which indicates that I-O-F units are the main sources to determine the magnitude of band gaps. When considering the equivalent replacement from O^{2-} to $2F^-$ in $CsIO_3$ and $CsIO_2F_2$, the experimental band gaps obviously increases from 4.25 to 4.56 eV, proving that the introduction of fluorine is beneficial for the blue-shift of bandgaps.[78] Among the four compounds, there are clear overlaps of the orbitals of I-p and O-p around -5 eV, identified as I-O covalent bonds, while the overlaps of I-*p* and F-*p* (I-F bonds) arise around the location of -2.5 eV. In addition, a sharp peak arises around -7 eV in O-p overlapped with H-*s* in the same energy location among $Cs(IO_2F_2)_2{\cdot}H_5O_2$, which is absent in the other three compounds, considered as the unique O-H bonds in the protonated $(H_5O_2)^+$ cations.

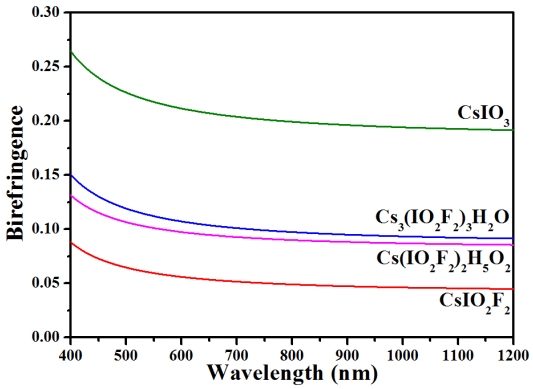

Figure 9. Birefringences of $CsIO_3$, $CsIO_2F_2$, $Cs_3(IO_2F_2)_3{\cdot}H_2O$ and $Cs(IO_2F_2)_2{\cdot}H_5O_2$.

As the birefringence reflects the optical anisotropy of a crystal, and also it is an essential qualification to achieve phase-matching, we plotted the birefringences of these four compounds through the first-principles calculations (Figure 9). Although these four compounds obtain similar element components, they exhibit hierarchical magnitudes in the optical anisotropy. $CsIO_3$ has the largest birefringence of 0.19 @1064 nm among them, while $CsIO_2F_2$ gets the smallest one (0.046 @1064 nm). $Cs_3(IO_2F_2)_3{\cdot}H_2O$ and $Cs(IO_2F_2)_2{\cdot}H_5O_2$ belong to different system of crystallization, orthorhombic and monoclinic, but show comparable birefringences, 0.093 and 0.086 @1064 nm, respectively. To further explore the sources of the optical anisotropy, the response electron distribution anisotropy (REDA) index is introduced, which is related with the distribution of the electronic density with covalent bonds.[79] And a higher REDA index reflects a stronger optical anisotropy. The calculated REDA index ratio of $CsIO_3$ and $CsIO_2F_2$ is $\zeta(CsIO_3) : \zeta(CsO_2F_2) = 2.3 : 1$, which is in accordance with the compared magnitude of their birefringences from DFT calculation. On the other hand, $Cs_3(IO_2F_2)_3{\cdot}H_2O$ and $Cs(IO_2F_2)_2{\cdot}H_5O_2$ have similar layered structures (Figure S5b and S5c in the SI), and their birefringences show little difference.

We employed the sum-over-states approximation at the static limit within the length gauge to estimate the NLO properties. Here, we chose the maximum SHG coefficient in the effective directions to assess the NLO responses, and the calculated results are 3.34 pm/V (8.6 KDP) for $CsIO_3$ and 2.75 pm/V (7.1 KDP) for $CsIO_2F_2$, in which the relative magnitude agrees with the experiments and is close to the results of other analogous metal iodate.[61] To explore the contribution of each atom for the SHG

responses in two compounds, we plotted the SHG densities in real space. Generally, there are two transition processes, virtual electron (VE) and virtual hole (VH) processes, contributing SHG response. Calculated results reveal that the VE processes are predominant (> 90%) in both $CsIO_3$ and $CsIO_2F_2$. As shown in Figure 10, the I and O atoms are the main sources of SHG responses in both $CsIO_3$ and $CsIO_2F_2$, and the contribution of the F atoms in $CsIO_2F_2$ is also significant, while cation Cs^+ contributes negligibly.

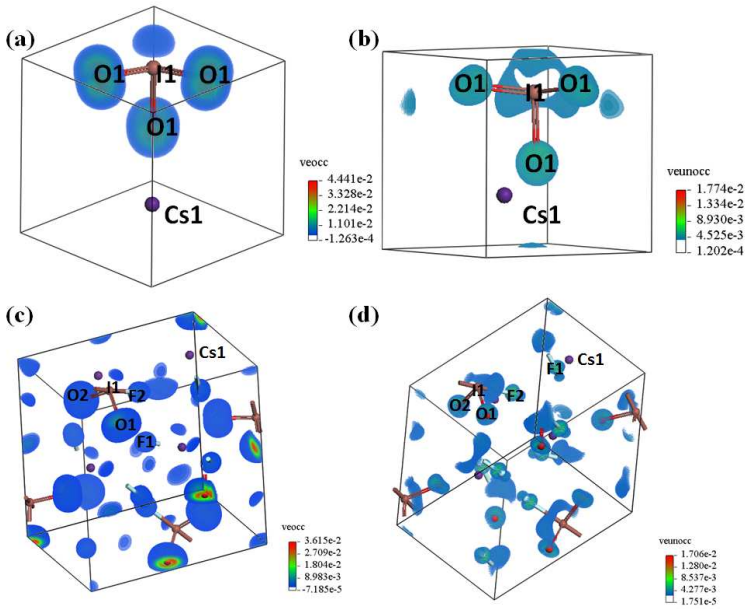

Figure 10. SHG densities of (a) (b) $CsIO_3$ and (c) (d) $CsIO_2F_2$: (a) (c) the occupied state, (b) (d) the unoccupied state.

CONCLUSION

The single crystals of $CsIO_3$ and other three new derivatives, $CsIO_2F_2$, $Cs_3(IO_2F_2)_3 \cdot H_2O$ and $Cs(IO_2F_2)_2 \cdot H_5O_2$ were successfully synthesized via hydrothermal method for the first time. Therein, $CsIO_3$ and $CsIO_2F_2$ have large SHG responses (15 and 3 times that of KDP) and wide transparency ranging from near-ultraviolet to mid-infrared. The wide experimental band gaps (4.2 and 4.5 eV) generate high LDTs (15 and 20 × $AgGaS_2$). The calculated birefringences for four compounds are 0.19, 0.046, 0.093 and 0.086 @1064 nm, respectively. The theoretical analyses from DFT calculations indicate that the introduction of the F atoms is beneficial for the blue-shift of band gaps and IO/F groups are the main sources of the

SHG effects based on the SHG densities in real space. The results indicate that $CsIO_3$ and $CsIO_2F_2$ are good candidates for the NLO applications, and the extremely large birefringence of $CsIO_3$ also makes it to be a promising birefringent material. The protonated $(H_5O_2)^+$ cations in $Cs(IO_2F_2)_2 \cdot H_5O_2$ implies that it may feature enhanced conductivity, which was tentatively verified by the resistivity tests via the conventional *dc* four-probe method. The attractive results propose a new structure-driven approach to design novel functional materials, and the researches of sizable crystal growths and further characterizations are still in progress.

ASSOCIATED CONTENT

The Supporting Information is available free of charge on the ACS Publications website. Atomic coordinates, equivalent isotropic displacement parameters and bond valence sums, selected bond lengths and angles, dipole moments of the IO_3/IO_2F_2 units, XRD patterns, resistivity tests, XRD patterns, band structures. CCDC number of four compounds are 1810691-1810694.

AUTHOR INFORMATION

Corresponding Authors

*E-mail: slpan@ms.xjb.ac.cn.

*E-mail: zhyang@ ms.xjb.ac.cn.

Notes

The authors declare no competing financial interest.

ACKNOWLEDGMENTS

This work was financially supported by Natural Science Foundation of Xinjiang, China (2017D01A75).

REFERENCES

(1) Sun, Y. Q.; Zhang, J.; Chen, Y. M.; Yang, G. Y. Porous Lanthanide–Organic Open Frameworks with Helical Tubes Constructed from Interweaving Triple-Helical and Double-Helical Chains. *Angew. Chem. Int. Ed.* **2005**, *44*, 5814–5817.

(2) Wang, X. F.; Wang, Y.; Zhang, B. B.; Zhang, F. F.; Yang, Z. H.; Pan, S. L. CsB_4O_6F: A Congruent-melting Deep-ultraviolet Nonlinear Optical Material by

Combining Superior Functional Units, *Angew. Chem. Int. Ed.* **2017**, *56*, 14119–1412.

(3) Yu, H. W.; Zhang, W. G.; Young, J.; Rondinelli, J. M.; Halasyamani P. S. Design and Synthesis of the Beryllium-Free Deep-Ultraviolet Nonlinear Optical Material $Ba_3(ZnB_5O_{10})PO_4$. *Adv. Mater.* **2015**, *27*, 7380–7385.

(4) Zhang, H.; Zhang, M.; Pan, S. L.; Dong, X. Y.; Yang, Z. H.; Hou, X. L.; Wang, Z.; Chang, K. B.; Poeppelmeier, K. R. $Pb_{17}O_8Cl_{18}$: A Promising IR Nonlinear Optical Material with Large Laser Damage Threshold Synthesized in an Open System. *J. Am. Chem. Soc.* **2015**, *137*, 8360–8363.

(5) Kang, L.; Zhou, M. L.; Yao, J. Y.; Lin, Z. S.; Wu, Y. C.; Chen, C. T. Metal Thiophosphates with Good Mid-infrared Nonlinear Optical Performances: A First-Principles Prediction and Analysis. *J. Am. Chem. Soc.* **2015**, *137*, 13049−13059.

(6) Dong, X. Y.; Jing, Q.; Shi, Y. J.; Yang, Z. H.; Pan, S. L.; Poeppelmeier, K. R.; Young, J.; Rondinelli, J. M. $Pb_2Ba_3(BO_3)_3Cl$: A Material with Large SHG Enhancement Activated by Pb-Chelated BO_3 Groups. *J. Am. Chem. Soc.* **2015**, 137, 9417–9422.

(7) Halasyamani, P. S.; Poeppelmeier, K. R. Noncentrosymmetric Oxides. *Chem. Mater.* **1998**, *10*, 2753−2769.

(8) Xia, Z. G.; Poeppelmeier, K. R. Chemistry-Inspired Adaptable Framework Structures, *Acc. Chem. Res.* **2017**, *50*, 222–1230.

(9) Mei, J. G.; Diao, Y.; Appleton, A. L.; Fang, L.; Bao, Z. N. Integrated Materials Design of Organic Semiconductors for Field-Effect Transistors, *J. Am. Chem. Soc.* **2013**, *135*, 6724−6746.

(10) Farha, O. K.; Hupp, J. T. Rational Design, Synthesis, Purification, and Activation of Metal−Organic Framework Materials. *Acc. Chem. Res.* **2010**, *43*, 1166–1175.

(11) Chen, S.; Slattum, P.; Wang, C. Y.; Zang, L. Self-Assembly of Perylene Imide Molecules into 1D Nanostructures: Methods, Morphologies, and Applications. *Chem. Rev.* **2015**, *115*, 11967−11998.

(12) Evans, O. R.; Lin, W. B. Rational Design of Nonlinear Optical Materials Based on 2D Coordination Networks. *Chem. Mater.* **2001**, *13*, 3009–3017.

(13) Ok, K. M. Toward the Rational Design of Novel Noncentrosymmetric Materials: Factors Influencing the Framework Structures. *Acc. Chem. Res.* **2016**, *49*, 2774–2785.

(14) Jo, H.; Oh, S. J.; Ok, K. M. Noncentrosymmetric (NCS) Solid Solutions: Elucidating the Structure–nonlinear Optical (NLO) Property Relationship and Beyond. *Dalton Trans.* **2017**, *46*, 15628–15635.

(15) Lu, H. C.; Gautier, R.; Donakowski, M. D.; Tran, T.T.; Edwards, B. W.; Nino, J. C.; Halasyamani, P. S.; Liu, Z. T.; Poeppelmeier, K. R. Nonlinear Active Materials: An Illustration of Controllable Phase Matchability. *J. Am. Chem. Soc.* **2013**, *135*, 11942−11950.

(16) Liang, F. Kang, L.; Gong, P. F.; Lin, Z. S.; Wu, Y. C. Rational Design of Deep-Ultraviolet Nonlinear Optical Materials in Fluorooxoborates: Toward Optimal Planar Configuration. *Chem. Mater.* **2017**, *29,* 7098–7102.

(17) Shi, G. Q.; Wang, Y.; Zhang, F. F.; Zhang, B. B.; Yang, Z. H.; Hou, X. L.; Pan, S. L.; Poeppelmeier, K. R. Finding the Next Deep-Ultraviolet Nonlinear Optical Material: $NH_4B_4O_6F$. *J. Am. Chem. Soc.* **2017**, *139*, 10645–10648.

(18) Zhou, B.; Yu, J. H.; Li, J. Y.; Xu, Y. H.; Xu, W. G.; Qiu, S. L.; Xu, R. R. Rational Design of Two-Dimensional Layered Aluminophosphates with $[Al_3P_4O_{16}]^{3-}$ Stoichiometry. *Chem. Mater.* **1999**, *11*, 1094–1099.

(19) Marvel, M. R.; Lesage, J.; Baek, J.; Halasyamani, P. S.; Stern, C. L.; Poeppelmeier, K. R. Cation-Anion Interactions and Polar Structures in the Solid State. *J. Am. Chem. Soc.* **2007**, *129*, 13963–3969.

(20) Mutailipu, M.; Xie, Z. Q.; Su, X.; Zhang, M.; Wang, Y.; Yang, Z. H.; Janjua, M.; Pan, S. L. Chemical Cosubstitution-Oriented Design of Rare-Earth Borates as Potential Ultraviolet Nonlinear Optical Materials, *J. Am. Chem. Soc.* **2017**, DOI: 10.1021/jacs.7b11263.

(21) Liu, B. W.; Zhang, M. Y.; Jiang, X. M.; Li, S. F.; Zeng, H. Y.; Wang, G. Q.; Fan, Y. H.; Su, Y. F.; Li, C. S.; Guo, G. C.; Huang, J. S. Large Second-Harmonic

Generation Responses Achieved by the Dimeric $[Ge_2Se_4(\mu\text{-}Se_2)]^{4-}$ Functional Motif in Polar Polyselenides $A_4Ge_4Se_{12}$ (A = Rb, Cs), *Chem. Mater.* **2017**, *29*, 9200−9207.

(22) Liu, X. M; Li, G. H.; Hu, Y. W.; Yang, M.; Kong, X. G.; Shi, Z.; Feng, S. H. Hydrothermal Synthesis and Crystal Structure of Polar and Nonpolar Compounds in Indium Iodate Family. *Cryst. Growth Des.* **2008**, *8*, 2453–2457.

(23) Xu, X.; Hu, C. L.; Li, B. X.; Yang, B. P.; Mao, J. G. α-AgI_3O_8 and β-AgI_3O_8 with Large SHG Responses: Polymerization of IO_3 Groups into the I_3O_8 Polyiodate Anion, *Chem. Mater.* **2014**, *26*, 3219−3230.

(24) Zhang, M.; Su, X.; Mutailipu, M.; Yang, Z. H.; Pan, S. L. $Bi_3OF_3(IO_3)_4$: Metal Oxyiodate Fluoride Featuring a Carbon-Nanotube-like Topological Structure with Large Second Harmonic Generation Response. *Chem. Mater.* **2017**, *29*, 945–949.

(25) Mao, F. F.; Hu, C. L.; Xu, X.; Yan, D.; Yang, B. P.; Mao, J. G. $Bi(IO_3)F_2$: The First Metal Iodate Fluoride with a Very Strong Second Harmonic Generation Effect. *Angew. Chem. Int. Ed.* **2017**, *56*, 2151–2155.

(26) Sun, C. F.; Hu, C. L.; Xu, X.; Ling, J. B.; Hu, T.; Kong, F.; Long, X. F.; Mao, J. G. $BaNbO(IO_3)_5$: A New Polar Material with a Very Large SHG Response. *J. Am. Chem. Soc.* **2009**, *131*, 9486–9487.

(27) Nguyen, S. D.; Yeon, J. H.; Kim, S. H.; Halasyamani, P. S. $BiO(IO_3)$:ANewPolar Iodate that Exhibits an Aurivillius-Type $(Bi_2O_2)^{2+}$ Layer and a Large SHG Response. *J. Am. Chem. Soc.* **2011**, *133*, 12422–12425.

(28) Suffren, Y.; Leynaud, O.; Plaindoux, P.; Brenier, A.; Gautier-Luneau, I. Differences and Similarities between Lanthanum and Rare-Earth Iodate Anhydrous Polymorphs: Structures, Thermal Behaviors, and Luminescent Properties. *Inorg. Chem.* **2016**, *55*, 11264−11272.

(29) Taouti, M. B.; Suffren, Y.; Leynaud, O.; Benbertal, D.; Brenier, A.; Gautier-Luneau, I. Structures, Thermal Behaviors, and Luminescent Properties of Anhydrous Lanthanum Iodate Polymorphs. *Inorg. Chem.* **2015**, *54*, 3608–3618.

(30) Wang, H.; Jian, G.; Zhou, W.; DeLisio, J. B.; Lee, V. T.; Zachariah, M. R. Metal Iodate-Based Energetic Composites and Their Combustion and Biocidal Performance. *ACS Appl. Mater. Interfaces* **2015**, *7*, 17363−17370.

(31) Sullivan, K. T.; Piekiel, N. W.; Chowdhury, S.; Wu, C.; Zachariah, M. R.; Johnson, C. E. Ignition and Combustion Characteristics of Nanoscale Al/$AgIO_3$: A Potential Energetic Biocidal System. *Combust. Sci. Technol.* **2010**, *183*, 285−302.

(32) Wang, W.; Huang, B.; Ma, X.; Wang, Z.; Qin, X.; Zhang, X.; Dai, Y.; Whangbo, M.-H. Efficient Separation of Photogenerated Electron-Hole Pairs by the Combination of a Heterolayered Structure and Internal Polar Field in Pyroelectric $BiOIO_3$ Nanoplates. *Chem. −Eur. J.* **2013**, *19*, 14777−14780.

(33) Huang, H. W.; He, Y.; He, R.; Lin, Z. S.; Zhang, Y. H.; Wang. S. C. $Y(IO_3)_3$ as a Novel Photocatalyst: Synthesis, Characterization, and Highly Efficient Photocatalytic Activity. *Inorg. Chem.* **2014**, *53*, 8114−8119.

(34) Muradyan, G. G.; Nalbandyan, A.G.; Sharkhatunyan, R.O. Dislocation Loops in Lithium Iodate Single Crystals. *J. Cryst. Growth* **1981**, *52*, 936–938.

(35) Kurtz, S. K.; Perry, T. T. The Powder Technique for the Evaluation of Nonlinear Optical Materials. *J. Appl. Phys.* **1968**, *39*, 3798−3813.

(36) Yin, X.; Lü, M. K.; Zhang, S. J.; Li, F. Q. Nonlinear Optical Properties of Perfectly Polarized KIO_3 Single Crystal. *Chin. Phys. Lett.* **1992**, *9*, 77−78.

(37) Kong, F.; Sun, C. F.; Yang, B. P.; Mao, J. G. Second-Order Nonlinear Optical Materials Based on Metal Iodates, Selenites, and Tellurites. *Struct. Bond.* **2012**, *144*, 43–104.

(38) Yang, B. P.; Hu, C. L.; Xu, X.; Sun, C. F.; Zhang, J. H.; Mao, J. G. $NaVO_2(IO_3)_2(H_2O)$: A Unique Layered Material Produces A Very Strong SHG Response. *Chem. Mater.* **2010**, *22*, 1545–1550.

(39) Sun, C. F.; Hu, C. L.; Xu, X.; Ling, J. B.; Hu, T.; Kong, F.; Long, X. F.; Mao, J. G. $BaNbO(IO_3)_5$: A New Polar Material with a Very Large SHG Response. *J. Am. Chem. Soc.* **2009**, *131*, 9486–9487.

(40) Sun, C. F.; Hu, C. L.; Xu, X.; Yang, B. P.; Mao, J. G. Explorations of New Second-Order Nonlinear Optical Materials in the Potassium Vanadyl Iodate System. *J. Am. Chem. Soc.* **2011**, *133*, 5561–5572.

(41) Belokoneva, E. L.; Dimitrova, O. V. New Triclinic Modification of Lead Iodate $Pb(IO_3)_2$: Synthesis and Crystal Structure. *Crystallogr. Rep.* **2014**, *59*, 174–178.

(42) Sun, C. F.; Hu, C. L.; Mao, J. G. $PbPt(IO_3)_6(H_2O)$: a New Polar Material with Two Types of Stereoactive Lone-pairs and a Very Large SHG Response. *Chem. Commun*. **2012**, *48*, 4220–4222.

(43) Halasyamani, P. S. Asymmetric Cation Coordination in Oxide Materials: Influence of Lone-Pair Cations on the Intra-octahedral Distortion in d^0 Transition Metals. *Chem. Mater.* **2004**, *16*, 3586–3592.

(44) Ravi Kumar, S. M.; Melikechi, N.; Selvakumar, S.; Sagayaraj, P. Crystal Growth and Characterization of Monometallic NLO Single Crystals of $Cd(IO_3)_2$. *J. Cryst. Growth* **2009**, *311*, 337–341.

(45) Yang, B. P.; Hu, C. L.; Xu, X.; Huang, C.; Mao, J. G. $Zn_2(VO_4)(IO_3)$: A Novel Polar Zinc(II) Vanadium(V) Iodate with a Large SHG Response. *Inorg. Chem.* **2013**, *52*, 5378–5384.

(46) Li, G. H.; Shi, Z.; Liu, X. M.; Dai, Z. M.; Gao, L.; Feng, S. H. A New Inorganic-Organic Hybrid Copper Iodate with Potentially Large Void Volume. *Inorg. Chem.* **2004**, *43*, 8224–8226.

(47) Chang, H. Y.; Kim, S. H.; Halasyamani, P. S.; Ok, K. M. Alignment of Lone Pairs in a New Polar Material: Synthesis, Characterization, and Functional Properties of $Li_2Ti(IO_3)_6$. *J. Am. Chem. Soc.* **2009**, *131*, 2426–2427.

(48) Chang, H. Y.; Kim, S. H.; Ok, K. M.; Halasyamani, P. S. Polar or Nonpolar? A^+ Cation Polarity Control in $A_2Ti(IO_3)_6$ (A = Li, Na, K, Rb, Cs, Tl). *J. Am. Chem. Soc*. **2009**, *131*, 6865–6873.

(49) Hu, C. L.; Mao, J. G. Recent Advances on Second-order NLO Materials Based on Metal Iodates. *Coord. Chem. Rev.* **2015**, *288*, 1–17.

(50) Mao, F. F.; Hu, C. L.; Li, B. X.; Mao, J. G. Acentric $La_3(IO_3)_8(OH)$ and $La(IO_3)_2(NO_3)$: Partial Substitution of Iodate Anions in $La(IO_3)_3$ by Hydroxide or Nitrate Anion. *Inorg. Chem.* **2017**, *56*, 14357–14365.

(51) Sykora, R. E.; Ok, K. M.; Halasyamani, P. S.; Albrecht-Schmitt, T. E. Structural Modulation of Molybdenyl Iodate Architectures by Alkali Metal Cations in $AMoO_3(IO_3)$ (A = K, Rb, Cs): A Facile Route to New Polar Materials with Large SHG Responses. *J. Am. Chem. Soc.* **2002**, *124*, 1951−1957.

(52) Yang, B. P.; Hu, C. L.; Xu, X.; Mao, J, G, New Series of Polar and Nonpolar Platinum Iodates $A_2Pt(IO_3)_6$ (A = H_3O, Na, K, Rb, Cs). *Inorg. Chem*. **2016**, *55*, 2481−2487.

(53) Xu, X.; Yang, B. P.; Huang, C.; Mao, J. G. Explorations of New Second-Order Nonlinear Optical Materials in the Ternary Rubidium Iodate System: Noncentrosymmetric β-$RbIO_3(HIO_3)_2$ and Centrosymmetric $Rb_3(IO_3)_3(I_2O_5)(HIO_3)_4(H_2O)$. *Inorg. Chem.* **2014**, *53*, 1756–1763.

(54) Kreuer, K. D. Proton Conductivity: Materials and Applications. *Chem. Mater.* **1996**, *8*, 610–641.

(55) Eigen, M. Proton Transfer, Acid-Base Catalysis, and Enzymatic Hydrolysis. *Angew. Chem. int. Ed.* **1964**, *3*, 1–19.

(56) Stoyanov, E. S.; Reed, C. A. IR Spectrum of the $H_5O_2^+$ Cation in the Context of Proton Disolvates L-H+-L. *J. Phys. Chem. A* **2006**, *110*, 12992–13002.

(57) SAINT, version 7.60A; Bruker Analytical X-ray Instruments, Inc.: Madison, WI, **2008**.

(58) Sheldrick, G. M. SHELXTL, version 6.14; Bruker Analytical X-ray Instruments, Inc. Madison, WI, **2008**.

(59) Spek, A. L. Single-crystal Structure Validation with the Program PLATON. *J. Appl. Crystallogr.* **2003**, *36*, 7–13.

(60) Kubelka, P.; Munk, F. Z. Ein Beitrag zur Optik der Farbanstriche. *Tech. Phys.* **1931**, *12*, 593–601.

(61) Wu, Q.; Liu, H. M.; Jiang, F. C.; Kang, L.; Yang, L.; Lin, Z. S.; Hu, Z. G.; Chen, X. G.; Meng, X. G.; Qin, J. G. $RbIO_3$ and $RbIO_2F_2$: Two Promising Nonlinear

Optical Materials in Mid-IR Region and Influence of Partially Replacing Oxygen with Fluorine for Improving Laser Damage Threshold. *Chem. Mater.* **2016**, *28*, 1413−1418.

(62) Kohn, W. Nobel Lecture: Electronic Structure of Matter—Wave Functions and Density Functionals. *Rev. Mod. Phys.* **1999**, *71*, 1253–1266.

(63) Clark, S. J.; Segall, M. D.; Pickard, C. J.; Hasnip, P. J.; Probert, M. I.; Refson, K.; Payne, M. C. First Principles Methods Using CASTEP. *Z. Kristallogr. - Cryst. Mater.* **2005**, *220*, 567−570.

(64) Perdew, J.; Burke, K.; Ernzerhof, M. Generalized Gradient Approximation Made Simple. *Phys. Rev. Lett.* **1996**, *77*, 3865−3868.

(65) Rappe, A. M.; Rabe, K. M.; Kaxiras, E.; Joannopoulos, J. D. Optimized Pseudopotentials. *Phys. Rev. B* **1990**, *41*, 1227−1230.

(66) Wang, C. G. The Crystal Structure of Cesium Iodate. *Acta Chim. Sinica*. **1985**, *43*, 271–274.

(67) Rogers, M. T.; Helmholz, L. The Crystal Structure of Iodic Acid. *J. Am. Chem. Soc*. **1941**, *63*, 278–284.

(68) Brown, I. D.; Altermatt, D. Bond-valence Parameters Obtained from a Systematic Analysis of the Inorganic Crystal Structure Database. *Acta Cryst.* **1985**, *B41*, 244–247.

(69) Brese, N. E.; O'Keeffe, M. Bond-valence Parameters for Solids. *Acta Cryst.* **1991**, *B47*, 192–197.

(70) Ryan, R. R.; Penneman, R. A. Presence of $H_5O_2^+$ in Erbium and Yttrium Oxalate-"Hydrogen Oxalate" Trihydrate. *Inorg. Chem.* **1971**, *10*, 2637–2638.

(71) Cotton, F. A.; Fair, C. K.; Lewis, G. E.; Mott, G. N. Ross, F. K.; Schultz, A. J.; Ic Williams, J. M. Precise Structural Characterizations of the Hexaaquovanadium (111) and Diaquohydrogen Ions. X-ray and Neutron Diffraction Studies of $[V(H_2O)_6][H_5O_2]CF_3SO_3)_4$. *J. Am. Chem. Soc*. **1984**, *106*, 5319–5323.

(72) Koch, E.; Fischer, W. Sphere Packings with Three Contacts Per Sphere and the Problem of the Least Dense Sphere Packing. *Z. Kristallogr. - Cryst. Mater.* **1995**, *210*, 407−414.

(73) Ok, K. M.; Halasyamani, P. S. New Metal Iodates: Syntheses, Structures, and haracterizations of Noncentrosymmetric $La(IO_3)_3$ and $NaYI_4O_{12}$ and Centrosymmetric β-$Cs_2I_4O_{11}$ and $Rb_2I_6O_{15}(OH)_2 \cdot H_2O$. *Inorg. Chem.* **2005**, *44*, 9353−9359.

(74) Cao, Z.; Peng, Y. X.; Yan, T. Y.; Li, S.; Li, A. L.; Voth, G. A. Mechanism of Fast Proton Transport along One-Dimensional Water Chains Confined in Carbon Nanotubes. *J. Am. Chem. Soc.* **2010**, *132*, 11395–11397.

(75) Levason, W. The Coordination Chemistry of Periodate and Tellurate Ligands, *Coord. Chem. Rev.* **1997**, *161*, 33–79.

(76) Wang, Y. X.; Duan, T.; Weng, Z. H.; Ling, J.; Yin, X. M.; Chen, L. H.; Sheng, D. P.; J. Diwu, Chai, Z. F.; Liu, N.; Wang, S. A. Mild Periodic Acid Flux and Hydrothermal Methods for the Synthesis of Crystalline f-Element-Bearing Iodate Compounds. *Inorg. Chem.* **2017**, *56*, 13041–13050.

(77) Niedner-Schatteburg, G. Infrared Spectroscopy and Ab Initio Theory of Isolated $H_5O_2^+$: From Buckets of Water to the Schrdinger Equation and Back. *Angew. Chem. Int. Ed.* **2008**, *47*, 1008–1011.

(78) Zhang, B. B.; Shi, G. Q.; Yang, Z. H.; Zhang, F. F.; Pan, S. L. Fluorooxoborates: Beryllium-Free Deep-Ultraviolet Nonlinear Optical Materials without Layered Growth. *Angew. Chem. Int. Ed*. **2017**, *56*, 3916−3919.

(79) Lei, B. H.; Yang, Z. H.; Pan, S. L. Enhancing optical anisotropy of crystals by optimizing bonding electron distribution in anionic groups. *Chem. Commun.* **2017,** *53*, 2818–2821.

Table 1. Crystallographic data for $CsIO_3$, $CsIO_2F_2$, $Cs_3(IO_2F_2)_3{\cdot}H_2O$ and $Cs(IO_2F_2)_2{\cdot}H_5O_2$.

Empirical formula	**$CsIO_3$ (1)**	**$CsIO_2F_2$ (2)**	**$Cs_3(IO_2F_2)_3{\cdot}H_2O$ (3)**	**$Cs(IO_2F_2)_2{\cdot}H_5O_2$ (4)**
Formula weight	307.81	329.81	1007.45	563.75
Temperature (K)	296(2)	296(2)	296(2)	296(2)
Wavelength (Å)	0.71073	0.71073	0.71073	0.71073
Crystal system	trigonal	orthorhombic	orthorhombic	monoclinic
Space group	*R*3*m* (No.160)	*Pca*2$_1$ (No.29)	*Pnma* (No.62)	*P*2$_1$/*c* (No.14)
a (Å)	6.6051(10)	8.781(3)	15.742(7)	4.476(4)
b (Å)	6.6051(10)	6.3771(18)	13.368(6)	7.968(8)
c (Å)	8.087(3)	8.868(3)	7.498(3)	13.790(13)
α (°)	90	90	90	90
β (°)	90	90	90	90.110(11)
γ (°)	120	90	90	90
Z	3	4	4	2
Volume (Å^3)	305.53(11)	496.6(2)	1578.0(12)	491.9(8)
Density (calcd) (g/cm^3)	5.019	4.411	4.241	3.806
Abs coeff (mm^{-1})	16.503	13.595	12.844	10.102
F(000)	396	568	1744	500
Cryst size (mm^3)	0.110×0.120×0.140	0.120×0.160×0.217	0.134×0.152×0.173	0.100 ×0.121 ×0.202
The range for data collection (deg)	4.36 to 27.17	3.19 to 27.67	2.59 to 27.70	2.95 to 27.53
Index ranges	$-8 \le h \le 8$, $-5 \le k \le 8$, $-8 \le l \le 10$	$-11 \le h \le 7$, $-8 \le k \le 8$, $-9 \le l \le 11$	$-20 \le h \le 19$, $-17 \le k \le 17$, $-9 \le l \le 8$	$-5 \le h \le 5$, $-7 \le k \le 10$, $-16 \le l \le 17$
Reflns collected/unique	625 / 179 [R(int) = 0.0156]	2809 / 1004 [R(int) = 0.0326]	9116 / 1916 [R(int) = 0.0312]	2785 / 1098 [R(int) = 0.0470]
Completeness (%)	100.0	99.7	99.3	97.3
Data/restraints/param	179 / 7/ 14	1004 / 1 / 56	1916 / 1 / 98	1098 / 3 / 69
GOF on F^2	1.266	1.064	1.008	1.082
Final *R* indices [$F_o^2 > 2\sigma(F_o^2)$][a]	R_1 = 0.0287 $wR2$ = 0.0657	R_1 = 0.0247 $wR2$ = 0.0352	R_1 = 0.0189 wR_2 = 0.0416	R_1 = 0.0568 wR_2 = 0.1223
R indices (all data)[a]	R_1 = 0.0287 $wR2$ = 0.0657	R_1 = 0.0304 $wR2$ = 0.0368	R_1 = 0.0256 wR_2 = 0.0450	R_1 = 0.0745 wR_2 = 0.1277
Flack parameter	0.6(2)	0.07(5)	/	/
Extinction coefficient	0.059(6)	0.00062(8)	0.00050(4)	0.0035(7)
Largest diff peak and hole (e/Å^3)	1.265 and -1.438	0.798 and -0.772	0.896 and -0.844	1.865 and -2.277

[a] $R_1 = \Sigma||F_o| - |F_c||/\Sigma|F_o|$ and $wR_2 = [\Sigma w(F_o^2 - F_c^2)^2 / \Sigma w F_o^4]^{1/2}$ for $F_o^2 > 2\sigma(F_o^2)$.

For Table of Contents Only